THE JOURNAL OF Ammonia Energy

Available online at

jae.cardiffuniversitypress.org

ISSN **2752-7735**
The Journal of Ammonia Energy 03 (2025) 014–031

Cardiff University Press | Gwasg Prifysgol Caerdydd

Flame and flow characteristics of lean premixed turbulent $NH_3/H_2/N_2$-air flames with increasing Karlovitz numbers

Li T[a*], Shi S[a], Schultheis R[a], Wang Z[b], Geyer D[c], Zhou B[b], Dreizler A[a]

[a] *Department of Mechanical Engineering, Technical University of Darmstadt, Otto-Berndt-Straße 3, Darmstadt, 64287, Germany.*
[b] *Department of Mechanics and Aerospace Engineering, Southern University of Science and Technology, No. 1088 Xueyuan Rd., Shenzhen, 518055,China.*
[c] *Optical Diagnostics and Renewable Energies, Darmstadt University of Applied Sciences, Haardtring 100, Darmstadt, 64295, Germany.*

Abstract

Premixed flames of partially cracked ammonia (NH_3) hold significant promise for the decarbonization of internal combustion engines and gas turbines, since they can burn at a similar laminar flame speed to methane but have notably high blow-out resistance. Understanding turbulent premixed flames with partially cracked NH_3 is highly relevant from both academic and application perspectives. This study aims to enhance our understanding of such premixed $NH_3/H_2/N_2$-air flames subjected to increasing turbulence. For this purpose, a specific fuel mixture, consisting of 40vol% NH_3, 45vol% H_2, and 15vol% N_2, is selected to match the laminar flame characteristics of methane at the same equivalence ratio. Turbulent jet flames are stabilized in a piloted burner with increasing bulk velocities from 30 to 180 m/s and Karlovitz numbers from approximately 75 to 2,140. One-dimensional (1D) simulations of freely propagating flames and strained counter-flow flames are performed, emphasizing temperature and species axial profiles and flame response to strain rate. Further, turbulent flow and flame structures are characterized using simultaneous particle image velocimetry (PIV) and laser-induced fluorescence of OH radicals (OH-LIF) measurements. Flame surface density Σ and curvature κ distributions are evaluated, revealing the dominant role of turbulence over differential diffusion in shaping the flame surface topology. It is also found that the OH intensity gradient ∇I_{OH} serves as a marker for local reactivity and thermo-diffusive instabilities, being higher at positive curvatures than at negative ones. Flat flames dominate the surface topology but show significant discrepancies in ∇I_{OH} as they appear both upstream and downstream of leading edges. The thickness of the OH layer is not broadened by turbulence, even at Ka = 2,140, suggesting that eddies cannot penetrate into the main reaction zone marked by OH radicals, which are formed at higher temperatures than the preheat layer.

Received: 16th Oct 24; Accepted: 10th Jan 25; Published: 11th April 25

Keywords: Premixed turbulent combustion, Ammonia and hydrogen, Flame and flow interaction, Laser combustion diagnostics.

1. Introduction

Hydrogen (H_2) has garnered significant attention from both fundamental and application-oriented research in recent years. Produced via water electrolysis using renewable electricity or through steam reforming combined with carbon dioxide (CO_2) capture and storage (CCS), clean H_2 is poised to play a crucial role in decarbonizing the existing energy supply system and achieving net-zero emission goals by replacing conventional fossil fuels [1]. As is well known, the widespread adoption of H_2 as an energy carrier is hindered by challenges related to its transportation and long-term storage. These challenges stem from hydrogen's inherent chemical and physical properties, including high diffusivity, low volumetric energy density, and explosive safety concerns. To address these issues, the development of efficient H_2 storage materials is vital for the sustainable utilization of renewable energy resources. Among the most promising H_2 carriers is ammonia (NH_3), which offers advantages in terms of energy density and ease of transport [2,3].

As an H_2 storage, NH_3 stands out with a gravimetric H_2 density of 17.8 wt%. NH_3 can be easily liquefied by compression at approximately 10 bar and room temperature. Importantly, NH_3 exhibits a very high volumetric H_2 density, approximately 1.6 times that of liquid H_2 and 3 times that of H_2 compressed at 700 bar. This characteristic offers the potential to reduce transportation and storage costs by up to 30% when compared to cryogenic H_2 [2]. To release stored energy in NH_3, direct burning pure NH_3 is considered an option, however, it is restricted by the

* Corresponding author. Tel.: +49-6151-28897. E-mail address: tao.li@rsm.tu-darmstadt.de
https://doi.org/10.18573/jae.37

low burning velocity, narrow flammability range, poor flame stability, and high NO_x emissions. Therefore, approaches such as non-equilibrium plasma-assisted combustion [4] and H_2 addition [2] are necessary to enhance the combustion properties. In particular, burning NH_3/H_2 blends or $NH_3/H_2/N_2$ blends (from NH_3 cracking) has been recently studied experimentally [5–8] and numerically [9–11].

Recently, a specific fuel mixture consisting of 40vol% NH_3, 45vol% H_2, and 15vol% N_2 attracted much research attention in the context of premixed turbulent combustion. This fuel mixture, denoted as AHNA-40/45/15, corresponds to about 43% pre-cracking of NH_3 (neglecting thermal effects) and will be focused on in this work. To understand this mixture, Fig. 1 shows the basic 1D flame characteristics of this mixture at various equivalence ratios obtained from freely propagating flame simulations, compared to pure NH_3-air and pure methane (CH_4)-air mixtures. More details about the simulations are given in Section 3. On the lean side, the adiabatic flame temperature T_{ad}, laminar flame speed S_L, and thermal flame thickness l_F (definition is given in Section 2) of AHNA-40/45/15-air is nearly equivalent to that of CH_4/air. However, the blow-out velocities or extinction limits increase up to a factor of 12 compared to the CH_4 [9]. This is presumably attributed to the preferential diffusion (H_2 diffuses faster than other species) and differential diffusion (mass diffuses faster than heat) at the less-than-unity Lewis number (*Le*) of this mixture, enhancing the turbulent fuel consumption speed. In addition, the NO formation is predicted to be significantly higher than pure NH_3 flames. To understand the enhanced stability and increased NO formation, an in-depth understanding of the macroscopic and microscopic flame structures in turbulent flows is an essential pillar for utilizing this mixture in practical combustion devices. Obtaining this knowledge requires laboratory-level turbulent flame and flow measurements with well-defined thermo-chemical boundary conditions and non-intrusive laser combustion diagnostics.

The turbulence-chemistry interaction (TCI) can be evaluated based on the Damköhler number (*Da*) and the Karlovitz number (*Ka* = 1/*Da*), which relate the chemical reaction timescales (or length scales) to the transport timescales (or length scales) in turbulent premixed combustion. The combustion regimes are commonly assessed using the Borghi-Peters regime diagram [12], as illustrated in Fig. 2. The cases investigated in the current study are identified by the coloured symbols in the regime diagram, and details will be discussed in Section 2. Different combustion regimes can be classified using u'/S_L, representing the ratio of turbulent velocity to laminar flame speed, and l/l_F, representing the ratio of integral length scale to flame thickness. For 1 <*Ka*< 100, the thin reaction zone regime exists, transitioning to the broken reaction zone or distributed combustion regime as *Ka* excesses 100. This regime diagram provides a fundamental basis for estimating the TCI in premixed turbulent combustion.

Experimental investigations on burner-type premixed turbulent flames of NH_3 and NH_3 blends have focused on turbulent flame speed S_T and flame structures. For instance, Cai et al. [8] measured the mean flame surface area (AT) of premixed NH_3/H_2 flames at high *Ka* up to 1,052 using laser-induced fluorescence (LIF) of NH radicals. Their results showed that the global consumption speed ($S_{T,GC}/S_L$) is significantly enhanced at *Le* < 1 due to the local intense burning caused by differential diffusion of H_2. Fan et al. [13] used simultaneous planar laser-induced fluorescence (PLIF) of NH and OH radicals to investigate NH_3/air turbulent flames with *Ka* up to 1,008. They reported that the NH layer thickness remains constant without broadening and the flame surface density obtained from NH and OH PLIF are similar. Ichikawa et al. [14] studied the burning velocity of CH_4/NH_3-air turbulent premixed flames under pressures up to 5 bar using OH-LIF. They found

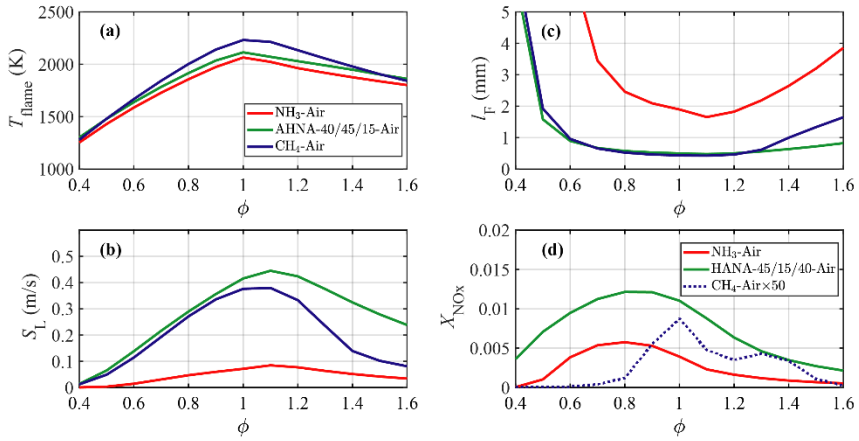

Fig. 1. Characteristics of 1D freely propagating flame of premixed NH_3-air, $NH_3/H_2/N_2$-air, and CH_4-air.

that the normalized turbulent flame speed (S_T/S_L) decreases with increasing NH_3 ratio at a constant u'/S_L, which is mainly attributed to the reduced flame surface density. Li et al. [15] developed multi-scalar diagnostics using simultaneous LIF of NH_3, NH, OH, and Rayleigh scattering to measure the flame speed of $NH_3/H_2/O_2/N_2$ turbulent premixed flames. By selecting different flame markers, they revealed quantitative discrepancies in S_T/S_L, implying different influences of differential diffusion on flame preheat and reaction zones. Wang et al. [16] applied the same diagnostics to study internal flame structures with varying Lewis numbers and turbulence levels. They found that both turbulence and H_2 content impact the parallelism of iso-contours of intermediate species. Schultheis et al. [5] experimentally quantified the internal structure of lean to rich premixed $NH_3/H_2/N_2$ flames using single-shot 1D Raman/Rayleigh spectroscopy. They reported the essential role of local oxygen concentration in modifying the molecular ratio of NH_3/H_2 in the temperature space, highlighting the relative importance of NH_3 depletion reactions versus oxidation reactions. In the rich flames, NH_3 depletes even before H_2 probably because the radial pool (e.g., H and NH_i radicals) generated during NH_3 decomposition inhibits the H_2 oxidation reactions.

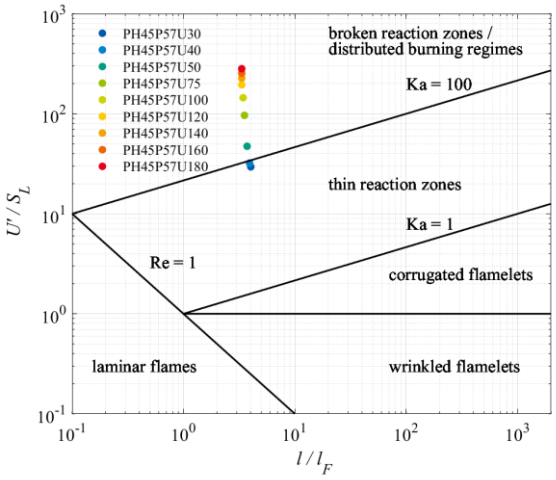

Fig. 2. Premixed combustion regime diagram by Borghi and Peters [12] and the flames investigated in the current study.

Although there have been increasing experimental efforts to understand NH_3/H_2 combustion for practical applications [2,3], only a few studies have focused on the detailed flame structures of premixed turbulent jet flames of partially cracked NH_3. In particular, the effects of differential diffusion and turbulence on local flame characteristics are not well understood. Key questions that remain unanswered include: How does turbulence modify the reaction zone structure of a thermo-diffusive flame? Is the main reaction zone of such a flame broadened at high *Ka*? How do differential diffusion and turbulence interact as flow timescales decrease? Besides, different levels of TCI can lead to a wide variety of local flamelet characteristics, making thorough flame characterization crucial for developing numerical tools for turbulent combustion of NH_3/H_2 blends. To address these scientific gaps, experimental data on turbulent premixed pre-cracked NH_3 flames are needed with well-defined boundary conditions. This will help improve our understanding of the interplay between differential diffusion and turbulence in modifying local flame structures and provide essential data for validating and developing advanced numerical models.

With this motivation, this work reports a comprehensive characterization of the premixed turbulent flame of 40vol% NH_3, 45vol% H_2, and 15vol% N_2 by using simultaneous OH-LIF and particle image velocimetry (PIV) measurements. Premixed flames are stabilized in a piloted jet burner with increasing bulk velocities, while the pilot is operated at the same H:N ratio as the jet mixtures. The effect of Karlovitz number (by varying the bulk velocity) on the macroscopic and microscopic flame structures is evaluated. The jet velocity is increased from 30 to 180 m/s at a constant equivalence ratio ϕ_{global} = 0.57, and the corresponding *Ka* rises from about 75 to 2,140. The equivalence ratio was selected to balance flame stability and comparability (i.e., similar laminar flame characters as methane flames), ensuring consistent results under the challenging flow conditions. The flame surface curvature distribution, flame surface density, gradients of OH radicals, and thickness of the OH layer are discussed.

In the following sections, the flame and flow conditions, along with optical diagnostics, are described in Section 2. Section 3 briefly discusses the strained 1D simulation of counter-flow flames to provide a basic understanding of an ideal flamelet's response to strain. The turbulent flow fields and macroscopic flame structures of the investigated flames are detailed in Sections 4.1 and 4.2, respectively. Sections 4.3 and 4.4 assess the OH gradient (representing local reactivity) and OH layer thickness (representing the thickness of the main reaction zone), respectively, in relation to the local flame surface curvature. Finally, the main findings are summarized in Section 5. To the best of the authors' knowledge, this paper provides the first analysis uncovering the response of OH gradients and OH layer thickness to increasing levels of turbulence in lean premixed $NH_3/H_2/N_2$/air jet flames with *Ka* up to about 2,140.

2. Experiments

2.1 Piloted fully premixed jet burner

To study the TCI of premixed $NH_3/H_2/N_2$-air (AHNA) turbulent flames, a piloted high-*Ka* jet burner (PHKB) was established to accommodate premixed combustion subject to different turbulence levels. Details of this burner have been given in previous work [5,17]; thus only the key features will be mentioned as follows. The burner, as schematically shown in Fig. 3, is composed of a central jet, an annular pilot, and an annular co-flow. The stainless steel jet nozzle has an inner diameter (D) of 4.5 mm and can be operated with a wide range of bulk gas velocities. The pilot flat flame is supported by a porous sintered stainless steel plate with an inner diameter (ID) of 6.3mm and an outer diameter (OD) of 60.5 mm, and a porosity of approximately 0.4, which is used to sustain the turbulent jet flame. The co-flow is fed through a porous sintered bronze plate (OD = 73.5 mm) to minimize air entrainment from the ambient environment. During the experiments, the co-flow is constantly operated with pure N_2 flow at a bulk velocity of 1 m/s. In addition, the pilot porous plug was water-cooled through an internal cooling coil at a constant temperature of 20°C, enabling constant thermal and aerodynamic boundary conditions.

2.2 Flame and flow conditions

In this study, the jet flame was operated with a fuel mixture of 40vol% NH_3, 45vol% H_2, and 15vol% N_2, which corresponds to a partial cracking of 43% of NH_3 under room temperature. As introduced previously, this mixture is of high academic and application interest since (i) it matches approximately the laminar flame speed of CH_4/air flames at the same equivalence ratio, making it as a well-suited benchmark, and (ii) it reveals much higher blow-out limits compared to CH_4/air flames in turbulent flows [9]. The high extinction resistance relies on the enhanced turbulent flame speed S_T, which not only scales up with turbulent velocity U', but is also significantly enhanced by the differential diffusion effect of H_2 [6,8].

Table 1 summarized the flame and flow conditions investigated in the current study. To vary the turbulence level, the jet bulk velocity (U_0) was increased from 30 to 180 m/s at a constant global equivalence ratio of 0.57. Note that there are two quasi-laminar cases with 10 and 20 m/s for comparison, which are not included but will be discussed in terms of the reaction zone thickness in Section 4.4. The flame cases are coded as PHαPβUγ, in which α, β, and γ refer to the H_2 volume fraction in the fuel, the global equivalence ratio, and the bulk gas velocity, in sequential order. The letter P indicates fully premixed flames, which differs to the stratified flame sets (S) presented in the previous experiment [5]. To guarantee the fully premixed combustion, the pilot flame was operated with lean H_2/N_2-air mixture containing 75vol% H_2 and 25vol% N_2 at the same equivalence ratio. This provides the same atomic ratio of H:N:O of jet and pilot and thus pure premixed combustion. This flame configuration is different to the previous Lund University Piloted Jet (LUPJ) flames [13,18] and our previous work [5], which are stratified flames with different mixtures in pilot and jet, in which chemical reactions occur in an intermediate range of equivalence ratios.

The pilot flame was operated with a relatively high bulk velocity of 2.5 m/s to produce a large cone-shaped exhaust region. Thus, jet flames at the largest bulk velocity were fully combusted within the pilot post-flame zone, eliminating additional dilution by the cold air from the environment.

To assess the turbulence-chemistry interaction, dimensionless turbulent Reynolds number Re_T and Karlovitz number *Ka* were evaluated. The laminar

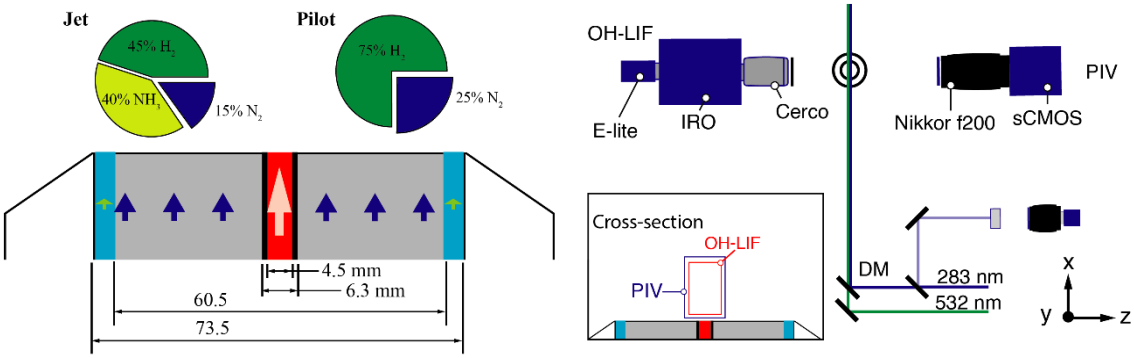

Fig. 3. (a) Sketch of the piloted fully premixed turbulent jet burner. (b) Optical setup of simultaneous OH-LIF and PIV measurements.

flame velocity S_L and thermal flame thickness l_F were obtained by simulating one-dimensional (1D) freely propagating flames. The 1D flame simulations were performed with a chemical mechanism reported by Han et al. [19] with a multi-component transport model and the Soret effect enabled. For the gas mixture used in the experiments, S_L is 11.2 cm/s and l_F is 1.02 mm, which is calculated based on the maximum temperature gradient $l_F = (T_{ad} - T_u)/|\nabla T|_{max}$, where the adiabatic flame temperature is T_{ad} = 1600 K and the unburnt gas temperature T_u is 300 K. Turbulent rms (root mean square) velocity magnitude U' and integral length scale l are evaluated from the measured turbulent velocity fields (more details will be given in Section 4.1). Using the parameters described above, Karlovitz number and turbulent Reynolds number can be calculated to characterize the TCI as follows [12],

$$Ka^2 = (\frac{U'}{S_L})^3 \frac{l_F}{l} \quad (1)$$

$$Re_T = \frac{U'l}{S_L l_F} \quad (2)$$

Due to the turbulence development and intense interaction between flow and flame, these values are significantly dependent on spatial locations under inspection. In Table 1, $U_C{}'$ and $U_F{}'$ represent the turbulent rms velocity at the jet center (subscript *C*) and in the flame region (subscript *F*), respectively. They represent the minimum and maximum turbulent velocity in the flame, respectively. Corresponding Karlovitz numbers Ka_C and Ka_F increases as turbulent intensity increased by elevating jet bulk velocity. Besides, the turbulent Reynolds number Re_T is calculated using the turbulent intensity for each flame case. Ka_C, and Ka_F were all determined at a downstream flame location of x = 7D. We note that selecting different radial or axial locations leads to significant discrepancy in l and U' values, which results in an ambiguity of dimensionless numbers including U'/S_L, l_F/l, Re_T, and *Ka*. This aspect is critical when placing premixed flames on the Borghi-Peters diagram by using a singular set of parameters to represent the entire flame. A different choice of parameters could lead to a transition to another combustion regime, and thus interpretations could be experimentally biased. Unfortunately, this aspect has been largely overlooked in the literature and some considerations are given in Section 4.1.

2.3 Simultaneous OH-LIF and PIV measurements

Flame and flow structures were assessed using simultaneous single-shot planar OH-LIF and PIV measurements. The experimental setup is schematically shown in Fig. 3. For OH-LIF, a frequency-doubled dye laser (Cobra-Stretch, Sirah) was pumped by a solid-state Nd:YAG laser (INDI, Spectra-Physics). The pump laser operated with an approximate output energy of 150 mJ at 532nm. The dye laser was tuned to λ = 283.01 nm, exciting the $Q_1(6.5)$ line of the A-X(1-0) transition. The laser beam was shaped into a 25 mm high sheet with a thickness of 120 µm (FWHM) using a combination of anti-reflection lenses and mirrors. This laser beam intersected the burner center line with an effective energy of 2 mJ/pulse. The LIF signals were collected by a CCD camera (Imager E-Lite 1.4M, LaVision) coupled with an intensifier (IRO X, LaVision). This detection system was complemented with a UV lens (Cerco, *f* = 100 mm, *f*/4) and a band-pass filter (305-340nm). The field of view (FOV) for OH-PLIF was 24 mm in height and 32 mm in width, with a pixel resolution corresponding to roughly 23 µm. The optical spatial resolution was estimated to be about 100 µm, which was then limited by the thickness of the laser sheet.

As shown in Fig. 3(b), a small portion of the UV laser was directed to a cell filled with ethanol dissolving a small amount of Rhodamine 6G. The emitted orange fluorescence signals were captured by another CMOS camera (Imager M-Lite 5M, LaVision). These 2D signals represented the energy distribution along the vertical direction of the laser sheet, which was then used to correct the sheet

Table 1. Flame and flow conditions of purely premixed $NH_3/H_2/N_2$-air turbulent jet flames.

Cases	ϕ_{global}	U_0 (m/s)	l (mm)	U'_C (m/s)	U'_F (m/s)	$Re_{T,F}$	Ka_C	Ka_F
PH45P57U30	0.57	30	4.1	1.8	3.3	128	30	75
PH45P57U40	0.57	40	4.0	2.6	3.6	140	50	85
PH45P57U50	0.57	50	3.8	3.1	5.3	204	65	150
PH45P57U75	0.57	75	3.6	4.5	10.8	410	115	425
PH45P57U100	0.57	100	3.5	5.9	16.2	623	175	795
PH45P57U120	0.57	120	3.4	7.0	21.8	833	225	1,230
PH45P57U140	0.57	140	3.4	8.1	25.4	972	280	1,550
PH45P57U160	0.57	160	3.4	8.8	28.5	1,087	315	1,830
PH45P57U180	0.57	180	3.4	9.7	31.6	1,205	365	2,140

Note: l, U'_C, U'_F, $Re_{T,F}$, Ka_C and Ka_F were determined for x = 7D.

inhomogeneity during the imaging processing steps. The OH-LIF images and beam cell images were spatially matched by imaging the dark streak caused by a thin wire to block a small portion of the laser beam.

For the simultaneous PIV measurements, a double-cavity Nd:YAG laser (PIV400, Innolas) was employed to produce double pulses with a 10 Hz repetition rate at 532 nm. The laser beams were spatially combined with the UV laser beam using a dichroic mirror (high reflection at 532 nm, high-transmission at 283 nm). The focused laser sheet was approximately 300 µm thick (FWHM) and the single pulse energy was about 4 mJ/pulse. The jet flow was seeded with aluminum oxide (Al2O3) particles (d_{50} = 1-1.7 µm) via a particle dispersion unit. The Mie scattering signals were captured using an sCMOS camera equipped with a Marco lens (Nikkor, f = 200 mm, f/22). A narrow band-pass filter (532 ± 3 nm) was employed to suppress interference from the background and flame luminescence. The projected pixel size for the PIV measurements was approximately 16 µm. The velocity vector fields were computed after smoothing (Gaussian filter, 5 × 5 pixels window size) and normalizing the particle images. Multi-pass processing was used with a window size of 32 × 32 pixels and 75% overlap in the final pass, resulting a vector spacing of about 128 µm. The estimated true spatial resolution was rather approximately 500 µm.

The excitation and detection systems for PIV and OH-LIF measurements were temporally and spatially synchronized. The PIV probe volume was slightly larger than that of OH-LIF, as indicated in the inset image in Fig. 3(b). The PIV pulses were separated by 2 µs to ensure reasonable pixel displacements in high-velocity jet flows, whereas UV laser pulses arrived approximately 500 ns ahead of the first PIV pulse. The burner was vertically moved to three different measurement positions, covering the flame height up to about x/D = 20, in which D is the jet diameter of 4.5 mm.

Through the evaluation of 600 instantaneous image pairs, statistical characteristics of turbulent reactive flows were derived. It is worth noting that velocity calculations in the jet post-flame region could be biased due to the absence of seeding particles in the pilot flame, where seeding particles through the porous material was prohibitive. Since vector computation relies on cross-correlation rather than tracking individual particles, local variation in particle seeding density can lead to a deterioration of correlation values. To address this issue, vector calculations were mainly restricted to the jet unburnt gas and reaction zone by masking out the pilot flame region. Subsequently, vectors with a peak ratio less than three were considered defective due to insufficient correlation quality and were excluded from the analysis. Furthermore, any interrogation window obtaining fewer than 2/3 independent vectors (i.e., 400 out of 600 vectors) was excluded to ensure statistical consistency. We believe these procedures significantly reduced experimental bias in vector field calculations.

3. Simulation of 1D flames

3.1 Unstrained flame and Lewis number

To obtain a basic understanding of the AHNA-40/45/15 mixtures, 1D freely propagating flame was simulated by applying a kinetic mechanism [19] in Cantera, including the multi-component transport model and Soret effect. Flame properties at varying equivalence ratios from 0.4 to 1.6 have been introduced in Section 1.

However, a H_2-enriched 1D flame responds to strain differently compared to a CH_4 flame, which is mainly due to the less-than-unity *Le* and the differential diffusion effect of H_2. Here, the dimensionless *Le* represents the relative rate of thermal diffusion and mass diffusion and can be calculated for individual species in mixtures using the equation proposed by [20],

$$Le = \frac{D_{th}}{D_m} = \frac{\lambda}{\rho \cdot c_p \cdot D_m} \quad \textbf{(3)}$$

where D_{th} and D_m represent the mixture thermal diffusivity and mass diffusivity of single species, respectively. The former is derived from the thermal conductivity λ, density ρ, and heat capacity c_p of the mixture. Accordingly, the Lewis numbers (*Le*) of NH_3, H_2, N_2, and O_2 are 1.21, 0.36, 1.25, and 1.27, respectively, at a temperature of 300 K. The volume-based *Le* of fuel mixtures can be calculated using $Le_{fuel} = \sum X_i Le_i$ by summing the Lewis numbers of each fuel species weighted by its mole fraction in the fuel mixture [21]. The effective *Le* of a fuel-oxidizer mixture is calculated as [22],

$$Le_{eff} = 1 + \frac{(Le_E - 1) + (Le_D - 1) \cdot \mathcal{A}}{\rho \cdot c_p \cdot D_m} \quad \textbf{(4)}$$
$$\mathcal{A} = 1 + Ze(\mathcal{K}_\phi - 1)$$

Le_D and Le_E denote the Lewis numbers of deficient and excessive reactants, respectively. $\mathcal{A}$ is a measure of mixing strength, derived from $\mathcal{K}_\phi$ and the Zeldovich number *Ze*. Here, $\mathcal{K}_\phi$ is the mass ratio of excess-to-deficient reactants, given by $\mathcal{K}_\phi = \phi$ for fuel-rich ($\phi > 1$) and $\mathcal{K}_\phi = 1/\phi$ for fuel-lean ($\phi < 1$) mixtures. The Zeldovich number is derived from the activation energy E_a, burnt and unburnt temperatures (T_b and T_u), and the universal gas constant $\mathcal{R}$ at pressure p, as shown in equations [12,20],

$$Ze = \frac{E_a(T_b - T_u)}{\mathcal{R} \cdot T_b^2} \quad \textbf{(5)}$$

and

$$\frac{E_a}{\mathcal{R}} = -2\left[\frac{\partial(\ln(\rho_u \cdot S_L))}{\partial(1/T_b)}\right] \quad \textbf{(6)}$$

ρ_u is the density of the unburnt gas mixture and S_L is the fuel consumption speed. By applying Equations (3)-(6), Ze and Le_{eff} are calculated for the fuel-oxidizer mixtures to be 13.6 and 0.87, respectively, for the investigated PH45P57 flames.

3.2 Strained flame

To achieve a further understanding of the strain effect on reaction zone structures, 1D flame simulations were conducted using an axis-symmetric premixed counter-flow configuration (reactants to products). This configuration partially mimics the experimental condition (from the jet to the hot pilot products) to a certain extent. The straining magnitude was modified by changing inlet gas velocities u. The strain rate K_s is computed as the maximum value of the velocity gradient $\partial u/\partial x$ to represent the strain of the flame. Fig. ***4*** showcases a representative result from such simulations along the axial direction (with the jet outlet at x = 0 mm) at a calculated strain rate of 1,000 s^{-1}.

In Fig. 4(a), it can be observed that u continuously reduces to its local minimum (indicated by the dashed line) before the temperature elevation and then increases afterward due to thermal gas expansion. The stretched flame speed S_b is computed by extrapolating u from the location of the maximum velocity gradient to the location of the maximum temperature gradient, which is considered as the reaction front (indicated by the red dashed line); at K_s = 1,000 s^{-1}, S_b = 0.19 m/s. In Fig. 4(b), the internal reaction zone structure is illustrated by displaying the mole fractions of H_2, NH_3, NH_2, NH, and OH, and heat release rate HRR, normalized on their respective maximum values. Due to differential diffusion, X_{H2} starts decreasing before X_{NH3} at a flame upstream location ahead of the pre-heat zone. As fuel is gradually consumed, NH_2 forms first a peak located close to the temperature gradient peak (refer to Fig. 4(c)), followed by NH at elevated temperature, however, with a much lower mole fraction. OH radicals form only at increasing temperatures together with the consumption of NH_2. Generally, NH_2 corresponds to the pre-heat zone at low-to-moderate temperatures, while OH represents the main reaction zone at elevated temperatures. Importantly, NH peak spatially aligns well with the HRR peak (dashed line), making it for these conditions the best HRR marker among other intermediate species. Fig. ***4***(c) compares the gradient of OH mole fraction $\partial X_{OH}/\partial x$ and temperature $\partial T/\partial x$, revealing a distance of 0.23 mm between their peaks (marked by vertical dashed lines). Compared to other species, OH radicals are located in regions with higher temperatures. As the fluid's viscosity increases with temperature, turbulence penetrating into the reaction zone will be degraded, thus imposing different levels of influence on the pre-heat and main reaction zones. The current work focuses on the influence on the main reaction zone marked by OH. For a direct comparison with the experiments, the $\partial X_{OH}/\partial x$ profile is used to characterize the main reaction thickness η_{OH} by calculating the full width at half maximum (FWHM). As a result, η_{OH} is approximately 0.3 mm for the freely propagating flame and decreases to 0.24 mm at K_s = 1,000 s^{-1}, and it is consistently smaller than the thermal thickness at all strain rates.

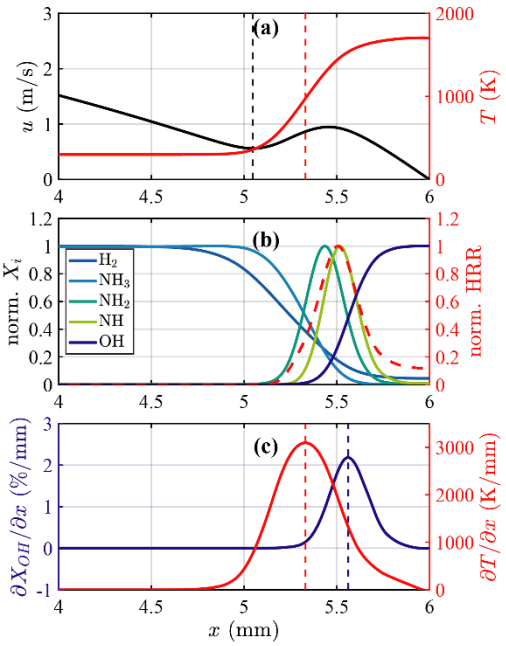

Fig. 4. 1D simulation profiles of (a) velocity u and temperature *T*, (b) normalized mole fraction of species and heat release rate, and (c) gradients of OH mole fraction and temperature.

The strain effect on flame structures is evaluated using the 1D simulation. In Fig. 5, S_b, η_{OH}, and the maximum flame temperature T_{max} are plotted over increasing strain rates K_s. For comparison, a CH_4/air flame is shown, and other two premixed flames with 60vol% H_2, 20vol% N_2 and 20vol% NH_3 (denoted as PH60P57) and 75vol% H_2 and 25vol% N_2 (denoted as PH75P57), respectively, are also computed to represent higher levels of NH_3 cracking.

Table 2. Gas mixtures used in 1D flame simulations.

Fuel mixtures	ϕ	X_{NH3}	X_{H2}	X_{N2}	Ze	Le_{eff}	Le_{fuel}	S_L (cm/s)
PH45P057	0.57	40	45	15	13.59	0.87	0.84	11.9
PH60P057	0.57	20	60	20	10.84	0.84	0.78	27.0
PH75P057	0.57	0	75	25	8.77	0.81	0.72	61.0

All simulations are performed at a constant equivalence ratio of 0.57. Calculated Le_{eff} and Le_{fuel} decrease as the H_2 mole fraction increases at a constant equivalence ratio. Table 2 summarizes the fuel mixtures used in 1D flame simulations in Cantera.

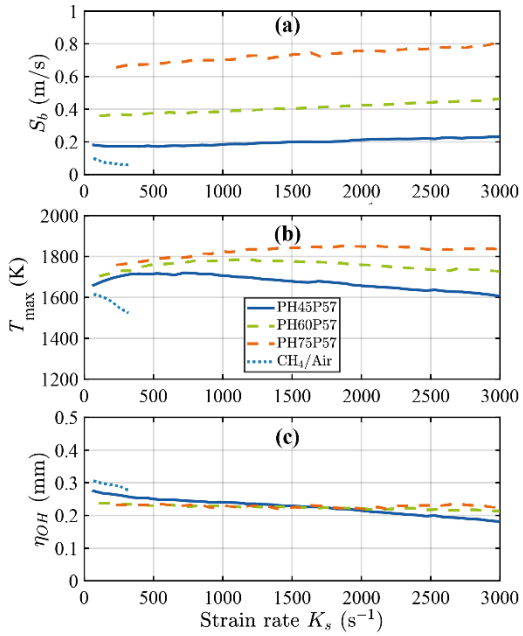

Fig. 5. 1D simulation results of premixed flamelet responding to increasing strain rate in an opposed jet simulation.

As shown in Fig. 5, strained burning velocity S_b of the lean $NH_3/H_2/N_2$-air mixtures slightly increases with strain rate, while a CH_4/air flame at the same equivalence ratio shows decreasing S_b with increasing strain. As it is widely known, the correlation between stretched and unstretched flame speed S_L^0 is given by $S_b = S_L^0 - S_L^0 \kappa L_c - K_s L_s$, where κ is the flame curvature, K_s is the strain rate, and L_c and L_s are Markstein lengths responding to curvature and strain, respectively [23]. Without the curvature effect included in the 1D counter-flow simulations ($\kappa = 0$), Fig. 5 (a) suggests a negative L_s, which is consistent with the theoretical correlation of burning velocity to the *Le* [23]. Fig. ***5***(b) indicates that, for H_2-containing flames, flame temperature first slightly increases and then decreases with strain rate, while it rapidly decreases for the CH_4/air flame. In Fig. 5(c), the representative OH layer thickness η_{OH} reduces at lower H_2 content (e.g., PH45P57), but remain relatively constant as H_2 fuel ratio increases (e.g., PH60P57 and PH75P57). The simulation results clearly show that (i) lean $NH_3/H_2/N_2$-air flames have a much higher strain resistance compared to CH_4/air flames at the same equivalence ratio, and (ii) increasing H_2 mole fractions in fuel leads to higher flame temperatures, larger burning speeds, and sustaining of the reactive layer thickness. Both effects relate to the differential diffusion and high reactivity of H_2 molecules.

4. Results and Discussions

4.1 Turbulent flow fields

Figure 6 presents a comparison of turbulent rms velocities U' (left-hand side) and the mean velocity magnitude U (right-hand side), normalized to the jet bulk velocity U_0, for premixed $NH_3/H_2/N_2$-air flames with increasing bulk velocity U_0 at a constant equivalence ratio of 0.57. The normalized mean velocity magnitude decreases rapidly along the radial direction, while turbulent velocity increases outwardly, reaching its maximum at about the outer edge of the jet nozzle (i.e, r/D = 0.5). The velocity difference between pilot exhaust gas and jet flow induces a shear flow with high turbulence intensity. Consequently, the shear flow zone enlarges and turbulent velocity increases as the jet bulk velocity increases, particularly at flow upstream locations. Moreover, more extensive velocity fluctuations are evident downstream as jet flow turbulence develops and interacts with the flame reaction zone.

To calculate Ka and Re_T in the axial and radial directions for the studied flame cases, the PIV measurement results enable determining turbulent rms velocities U' and integral length scales l. However, both parameters vary in axial and radial directions. Figure 7 illustrates radial profiles of (a) the mean axial velocity magnitude U and (b) turbulent rms velocities U' for lean $NH_3/H_2/N_2$-air flames with increasing jet bulk velocity from 30 to 180 m/s at a flame location of x/D = 7. The mean flow velocity exhibits a bell-shaped distribution profile along the radius. The integral length scale l can be estimated using the half-width at half- maximum (HWHM) of

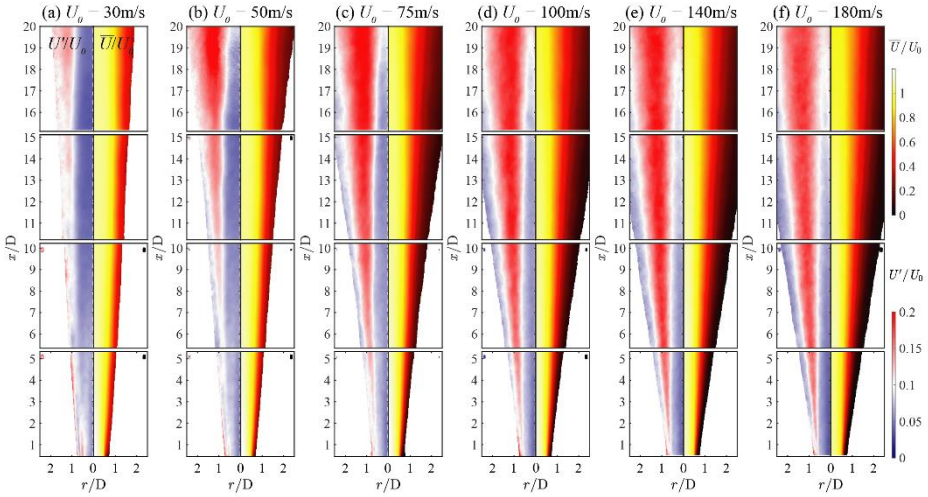

Fig. 6. Side-by-side comparison of normalized turbulent rms velocity U'/U_0 (left-hand side) and mean velocity magnitude U/U_0 (right-hand side) of purely premixed $NH_3/H_2/N_2$-air flames (PH45P57) with increasing bulk velocity U_0.

the mean velocity profile, and the values are listed in Table 1. U' shows relatively small values at the jet center, increasing with radius and peaking approximately at the flame surface positions, discussed in Section 4.2. To estimate the range of *Ka* numbers, the minimum U' at the centerline of the jet ($U_c{}'$) and the maximum U' in the flame ($U_F{}'$) are derived from velocity profiles. These values and the corresponding Karlovitz numbers Ka_C and Ka_F are listed in Table 1.

There are inherent uncertainties in determining the Karlovitz number, which characterizes the ratio between flame thickness l_F and the Kolmogorov length scale η. One critical consideration is that η represents the turbulence length scale to which a flamelet is subjected. When applying Equation (1), U' and l should properly reflect the turbulence at the location of the flame reaction zone. Therefore, utilizing U' at the jet centerline is improper, as it underestimates the turbulence level. However, using $U_F{}'$ might overestimate the turbulence since velocity fluctuations can partly stem from unsteady flame positions. Consequently, Ka_T and Re_T calculated using $U_F{}'$ should be interpreted as upper limits rather than exact values. A potentially more reasonable estimation involves statistical analysis of velocity conditioned on the flame front edge.

Additional uncertainties in estimating *Ka* stem from the accuracy of S_L and l_F, which heavily rely on the reaction kinetic mechanism. Particularly, obvious discrepancies exist in available mechanisms for NH_3 reactions [24,25]. While these uncertainties fall beyond the scope of this paper, they warrant more detailed analysis in future work. Special attention has to be paid to the accuracy of *Ka* when inspecting the Borghi-Peters regime diagram.

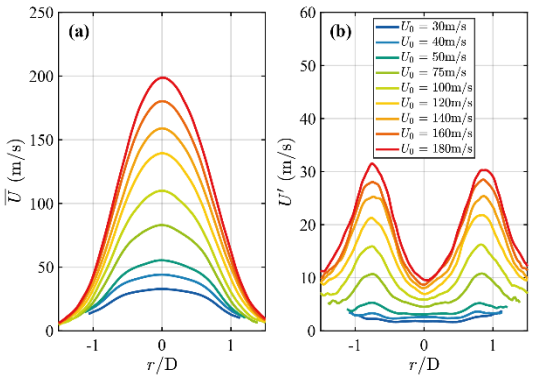

Fig. 7. Radial profiles of normalized velocity magnitude and turbulent intensity at *x*/D = 7 of purely premixed $NH_3/H_2/N_2$-air flames with increasing bulk velocity U_0.

4.2 Flame macroscopic structures

Figure 8 presents a side-by-side comparison of time-averaged mean (left-hand side) and instantaneous (right-hand side) OH-LIF intensities I_{OH} as the jet bulk velocity U_0 increases from 30 to 180 m/s. In general, the high OH-LIF intensity gradient between jet reactants and pilot exhausts can well present the main reaction zone of the jet flames, while the OH-LIF intensity in the pilot flame, due to the presence of high temperature, is at a background level. The flames appear different from the previously studied stratified flames [5] of richer $NH_3/H_2/N_2$-air mixtures, in which reactions occur together with mixing with additional oxidizer and OH is not a marker to represent the entire reaction zone.

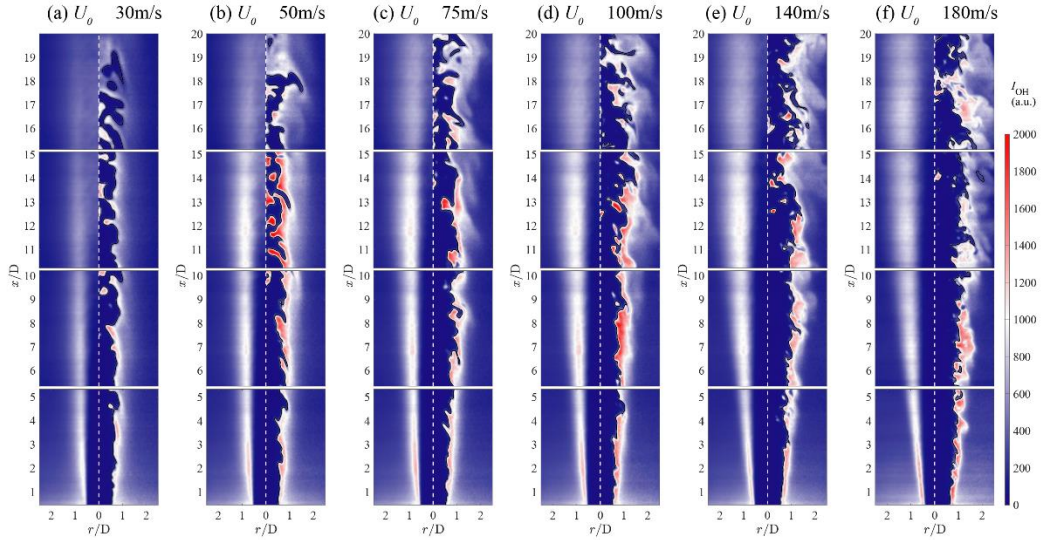

Fig. 8. Side-by-side comparison of mean and single-shot OH-LIF images of purely premixed $NH_3/H_2/N_2$-air flames with increasing bulk velocity U_0.

At the lean side, OH correlates well with the HRR zone, however, according to the 1D diffusion flame simulations NH radicals represent the HRR zone more reliably. As expected from Fig. 8, a higher U_0 results in an increased flame height and an expanded flame size in radial direction. At low turbulence, flame surface reveals moderate wrinkling induced by large-scale eddies. As U_0 increase, flame reaction zones become strongly disturbed, resulting in smaller-sized local structures and larger curvatures. This is because increased U' leads to smaller eddies with sufficient turbulent kinetic energy to disturb the thermal layer or even the main reaction zone. Local OH-LIF intensity increases with U_0 to a certain extent, in particular between x/D = 6-15, and is then gradually lowered with increased turbulence levels at jet downstream.

To inspect flame structure more closely, zoom-in images of single-shot OH-LIF intensities I_{OH} and corresponding gradient maps ∇I_{OH} are shown in Fig. 9, using examples from flame cases with U_0 = 30, 100, and 180 m/s. Here, the gradient is computed as a variation magnitude of intensity per unit length. We note that, despite the non-linear relation between the OH number density and fluorescence signal, both I_{OH} and ∇I_{OH} are proper markers to visualize the main reaction zone, while the later can be used as a marker for the thermo-diffusive instability [26]. The flame surface is detected using a gradient-based edge detection method, similar to the one reported by [27]. This method binarizes OH-LIF intensities using self-adapted thresholds and extracts flame edges approximating the location of the maximum intensity gradient. Moreover, the local flame curvature κ is evaluated using the algorithm proposed by [28]. The flame normal vectors are firstly computed by determining the direction of intensity gradients on each pixel of the flame front. Then, the principal curvatures κ_1 and κ_2 are evaluated through invariants of the curvature tensor.

For two-dimensional flame structures, flame curvature is the projected mean of two principal curvatures κ_1 and κ_2. Positive curvature is associated with the convex surface towards unburnt reactants, and negative curvature is associated with the concave surface towards burnt gas. Intensity and gradient images are superposed with detected flame edges color-coded by local surface curvatures.

Local flame structures reveal a wide variation of surface curvatures between positive (reddish) and negative (blueish) values, as shown in Fig. 9(a1-c1). At low turbulence level, local intense burning regions with high OH-LIF intensities are observed near the positively curved flame surface (highlighted with arrows in white), while reduced intensities are correlated with negatively curved surface. This is mainly caused by the differential diffusion of H_2, leading to thermo-diffusively unstable flame structures. With less-than-unity *Le*, the mass and thermal diffusion is imbalanced near a curved surface. Slower thermal diffusion (from burnt to unburnt) and faster mass diffusion (from unburnt to burnt) leads to enhancement (or suppression) of reactivity at positively (or negatively) curved reaction zone [29]. Recent 1D Raman/Rayleigh measurements reported that intense burning regions have higher equivalence ratio, higher H_2O mole fraction, and super-adiabatic flame temperature in premixed H_2/air flames [17].

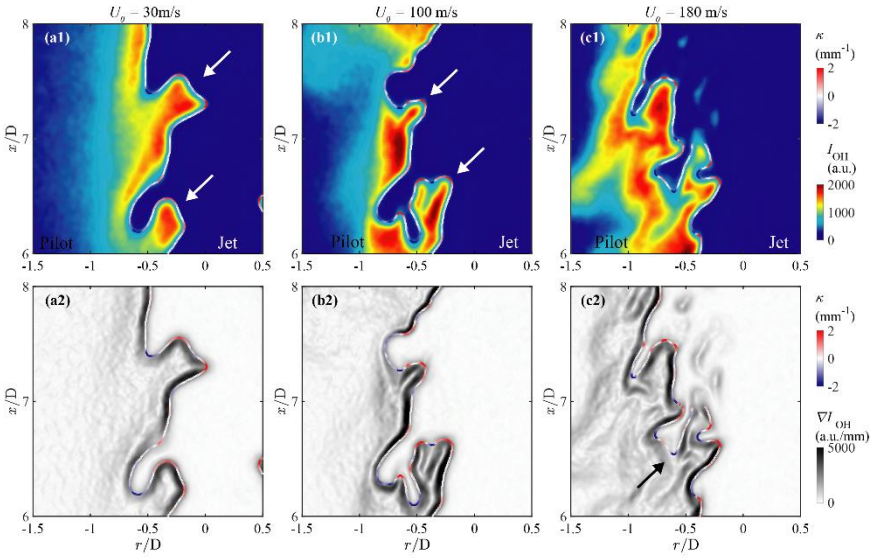

Fig. 9. Single-shot OH-LIF intensity I_{OH} in (a1-c1) and intensity gradient maps ∇I_{OH} (a2-c2), which are superposed with detected flame edges color-coded by curvatures κ.

As turbulence is increased by elevating the bulk velocity to 100 m/s, local intense burning regions are enhanced in the selected example, as flame surfaces are more intensively curved. This indicates that wrinkling, which is dominated by turbulence, intensifies the fuel and heat accumulation triggered by the differential diffusion effects. Further increasing turbulence by operation with a bulk velocity of 180 m/s, the clear correlation between intense burning regions and curvatures cannot be observed, and the flame zones are extensively disturbed by flow turbulence. The turbulent diffusion is playing a more significant role by distributing mixtures and heat at a faster rate (smaller turbulent time scales), thus suppressing the thermo-diffusive effect (controlled by molecular and thermal diffusion) and formation of super-adiabatic hot spots. These observations suggest that at moderate levels of turbulence, the interaction between turbulence and differential diffusion is synergistic, whereas at high levels of turbulence, local flame structures are dominated by turbulent transport; this observation is consistent with findings for premixed H_2/air flames with less-than-unity Le numbers in previous DNS [30] and quantitative measurements [30].

OH-LIF intensity gradients ∇I_{OH} are significantly influenced by the turbulence, as shown in Fig. 9(a2-c2). At a low turbulence level at U_0 = 30 m/s, high ∇I_{OH} are mostly restricted to a narrow region close to the flame surface, while ∇I_{OH} is much lower in the post-flame zone due to the homogeneous temperature distribution in the pilot exhaust gas. Here, small turbulent eddies with length scales similar to the flame thickness are not able to penetrate into the flame zone due to their low kinetic energy. As turbulence is increased at U_0 = 100 and 180 m/s, finer spatial structures in the gradient map are observed in the flame downstream location. In particular for U_0 = 180 m/s, ∇I_{OH} shows a substantial variation in magnitude. The corresponding image in Fig. 9(c1) clearly exhibits a broader zone associated with high OH-LIF intensities. At this turbulence level, turbulent eddies with higher kinetic energy may penetrate into the reaction zone, stretching fluid elements at high temperature and OH-LIF intensity, before their turbulent kinetic energy is dissipated by the increased gas viscosity due to thermal dilatation. At a disturbed flame zone marked by the black arrow in Fig. 9(c2), a discontinuity of OH gradients is observed, indicating a possible transition towards the broken reaction zone or distributed burning regime [31].

Inspecting local flame wrinkling in Fig. 9, another important aspect is that the highest value of ∇I_{OH} do not always appears at the tip or the leading point of positively curved flame edges (reddish colored). On the contrary, these values frequently appear close to regions with low surface curvature values (whitish color). This observation seems contrary to the conventional understanding of thermo-diffusive effects; thus, further discussion on the reaction zone intensity and flame thickness is continued in Section 4.3.

The flame surface detection provides the opportunity to compute the apparent flame surface density (FSD) Σ in its 2D projection, which is an essential parameter for the assessment of the local fuel consumption speed and turbulent burning velocity. To determine FSD, a control area (CA) with a size of Δx^2 is defined for Σ calculation according to [33]. The flame length P within each CAs is first

calculated, and the flame surface density is then given by $\Sigma = P/\Delta x^2$. Here, Δx = 1.04 mm is used, corresponding to 45 pixels. This fulfills the required size of CA, namely $\Delta x > l_F$, in which the laminar flame thickness l_F = 1.02 mm is obtained by the 1D simulation of a freely propagating flame. Fig. **10**(a1-c1) shows mean FSD Σ maps averaged over 600 single-shot images at representative *x*/D locations at increasing U_0 = 30, 100, and 180 m/s. At a lower flame height, two flame branches with clear Σ peaks are evident. Here, the flame front is less curved and remains mostly within a few CAs. The flame surface spreads downstream into more CAs. Due to stronger turbulent fluctuations, the radial distribution Σ becomes broader and Σ magnitudes reduce. Flame surface density is in the same order of magnitudes among flames with different jet velocities. These results clearly suggest that turbulent flows significantly impact the spatial distribution of the reaction zone. By integrating the 2D Σ along the normal direction of the mean flame brush [32], turbulent fuel consumption rate can be analyzed in future work.

Figure 10(a2-c2) shows the probability density functions (PDF) of the 2D curvature κ along the flame radial direction at different *x*/D locations of 3.5, 7, 10.5, and 14D. At a low bulk velocity of U_0 = 30 m/s, the κ peak slightly decreases in the axial direction and the distribution broadens with *x*/D due to increasing velocity fluctuations. This is consistent with Fig. 8(a), in which large-scale flame wrinkling appears downstream. At higher U_0 of 100 and 180m/s, the axial difference in κ-PDF decreases and the distribution curves overlap. This is because flame curvatures are determined by large eddies with comparable length scales, and turbulence intensity and U_F' only slightly increase with the flame height (see Fig. 6(d) and (f)). Moreover, we note that the κ-PDFs reveal symmetric distributions without any indications on skewness towards positive curvatures, different to previous thermo-diffusively unstable flames [26] with much smaller fuel *Le* numbers. With increasing turbulence intensities given by higher bulk velocities, the PDF distribution of κ broadens in both negative and positive directions. This suggests the flame curvatures are largely dominated by turbulence and insignificantly modified by differential diffusion effect, as the effective *Le* of mixture is close to unity (i.e., 0.87).

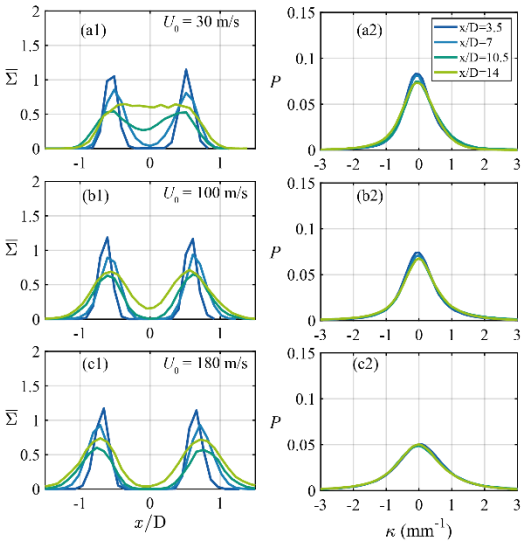

Fig. 10. (a1-c1) Mean flame surface density Σ and (a2-c2) probability density functions (PDF) of surface curvature κ of purely premixed $NH_3/H_2/N_2$-air flames at *x*/D = 3.5, 7, 10.5, and 14.

4.3 Local flame reactivity

Inspection of Fig. 9 shows that while the center of the positively curved flame has significantly higher OH intensity in the post-flame zone, positive curvatures at the tip of the leading edges are not directly associated with high OH gradients. Conversely, OH gradients near a flat flame surface are frequently higher than in curved regions. To gain further insight into this phenomenon of the present lean $NH_3/H_2/N_2$-air flames, we examine the local flame structure in another representative example at U_0 = 50 m/s. At this relatively low turbulence level, thermo-diffusive effects are pronounced, enabling the inspection of local variations in reactivity depending on flame topology. In this example, Fig. 11(a,b) zoom into a region around *x*/D = 7, where the intensity I_{OH} and the gradient ∇I_{OH} are illustrated. Again, these scalar images are superimposed with flame edges color-coded by the local 2D curvature value. Detected flame edges are smoothed using a Savitzky-Golay filter [33], and the flame normal vectors (arrows in black) are computed, pointing in a direction from unburnt to burnt gas.

Four inspection areas are selected, corresponding to negatively curved (1), positively curved (2), and flattened flame structures (3 and 4). These areas are denoted as κ^-, κ^+, and κ^0 to indicate the local flame topology categories. Specifically, corresponding curvature values are -3.7, 3.5, 0.2, and -0.3 mm^{-1} in the selected zones 1 to 4, respectively. Two flat surfaces are chosen because, although the absolute κ values are similarly low, they exhibit discrepancies in I_{OH} and ∇I_{OH} in the post-flame zone. Figure

11(c,d) show I_{OH} and ∇I_{OH} profiles along the flame surface normal direction $x \perp F$ ($x \perp F$ = 0 mm represents the location of the detected flame edge). In line with observations from Fig. 11(a,b), these profiles confirm that a negatively curved flame (blue line) is associated with lower I_{OH} and ∇I_{OH} compared to a positively-curved flame (red line). However, differences are observed between the two flat flame structures (black vs. gray line), where their ∇I_{OH} is even higher than the positively curved flame in area 2.

The observed flame characteristics on the instantaneous local structures are not incidental but rather indicative of interactions between turbulence and differential diffusion, which conjointly influence the reaction zone topology marked by OH radicals. To further elucidate this, joint probability density functions (JPDFs) of the intensity gradient and curvature are computed, conditioned on the flame front ($x \perp F$ = 0 mm). As demonstrated previously in Fig. 11(d), the detected flame front ($x \perp F$ = 0 mm) effectively represents the location of the maximum intensity gradient, a qualitative marker for the local reactivity. The curvature is normalized by the flame thickness l_F of the corresponding freely propagating

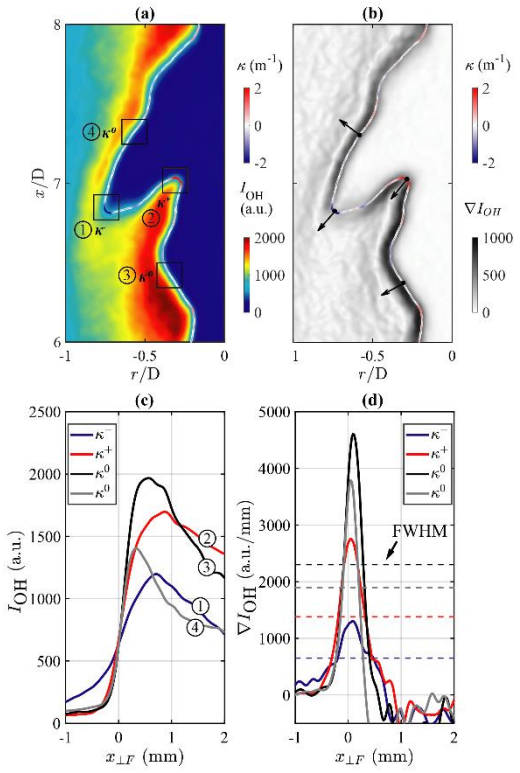

Fig. 11. Single-shot images of (a) OH-LIF intensity I_{OH} and (b) intensity gradient ∇I_{OH} superposed with flame front edges colored by local 2D curvature κ. Local profiles of (c) I_{OH} and (d) ∇I_{OH} along flame surface normal direction in the selected flame zones.

flame to represent the local flame topology. Accordingly, Fig. 12 presents the correlation of local reactivity and topology of the investigated premixed $NH_3/H_2/N_2$-air flames at x/D = 7 for increasing bulk velocities from 30 to 180 m/s at a constant equivalence ratio of 0.57. It is worth noting that the absolute probability value P depends on the binning width for ∇I_{OH} and $\kappa \cdot l_F$, and therefore only a qualitative comparison is intended.

Figure 12 suggests that the majority of local flame front structures exhibit a flattened surface, as indicated by the peaks near $\kappa \cdot l_F$ =0. Low curvatures dominate the reaction surface topology in flames that are influenced by thermo-diffusive effects, a phenomenon also observed in DNS studies for H_2/air flames [34] and experiments [26]. Increased turbulence resulting from elevated U_0 leads to wider probability distributions, as flame zones become more wrinkled by turbulent eddies. The skewness of the JPDF, which indicates that positive curvatures have higher ∇I_{OH} than negative curvatures, aligns with the single-shot observations in Fig. 9. The skewness can be observed in the mean curves of ∇I_{OH} (red lines). ∇I_{OH} is widely scattered at flat surfaces, even more so compared to curved surfaces, because similarly flat surfaces frequently relate to different local reactivity, as depicted in Fig. 9. The high probability of flat surfaces, the skewness of the JPDF, and the large scatter of ∇I_{OH} at flat surfaces are consistently observed across different bulk velocities and turbulence levels. Two observations/questions warrant further discussion: (i) why is the local reactivity (represented by ∇I_{OH}) higher at positively curved flames compared to their negatively curved counterparts, and (ii) why do flat flames scatter across a wide range of different local reactivities?

The first question can be elucidated by considering the differential diffusion effect of fuel mixtures with a *Le* less than unity [29]. A positively curved surface leads to the concentration of fuel and heat, resulting in locally modified heat release rates. Under globally lean conditions, an increase in equivalence ratio leads to a flame propagating faster and associated with higher temperatures. This is associated with larger scalar gradients across the reaction zone, enhancing as well ∇I_{OH}. DNS studies show that the local consumption speed is particularly high at positive curvatures [34], and these hot spots could significantly increase the global fuel consumption rate in thermo-diffusively unstable flames. However, the effects of differential diffusion can be mitigated by turbulence as the *Ka* exceeds a critical value [35]. This occurs because the turbulent timescale becomes shorter than the chemical timescale, leading to a mixing process dominated by rapidly redistributing

fuel and oxidizer through convection. As a result, the impact of differential molecular diffusion diminishes in the internal flame structures, and the flame transitions to a distributed burning regime or broken reaction zone [17]. The transition and the required Ka number depend on the fuel mixture and equivalence ratio. For highly diffusive lean H_2-air flames, the critical *Ka* could exceed several thousand, as reported by DNS [35] and quantitative scalar measurements [30]. In the current $NH_3/H_2/N_2$ mixture, a leveling of the PDF skewness is observed at U_0 = 180 m/s (corresponding *Ka* is about 2,140), suggesting a transition towards the suppression of differential diffusion effects. ∇I_{OH} is a suitable marker for thermo-diffusive instabilities and turbulence-chemistry interaction in less-than-unity *Le* flames.

The second question regarding the disparity in local reactivity at flat surfaces can be interpreted based on the influence of the leading point on the post-flame zone. Here, leading points refer to 2D structures with high positive curvature (e.g., zone 2 in Fig. 9), which could be either a point or an edge in three-dimensional space. These structures can be formed by large-scale turbulent eddies; however, they can also be extinguished under extreme strain and curvature conditions. The shape of leading edges is determined by the local competition between convection and extinction limits, while the latter can be extended by differential diffusion. This theory could explain why lean H_2/air flames can be strongly disturbed to form finger-like structures. Conventionally, the global fuel consumption rate in premixed combustion is thought to be largely determined by critical leading edges, as reviewed by [36]. An essential aspect is that, after the leading point has passed, it leaves behind a super-adiabatic region. Recent studies reveal that flame speed arises at low curvature due to the formation of a previous leading edge [34]. Therefore, leading edges can promote a nearly-flat flame with reaction rates higher than the reference 1D steady flat laminar flame [34]. This claim is supported by the current experiments, as shown in the single-shot visualization in Fig. 9, which shows higher reactivity with a flat flame in the wake of a leading edge. It is also consistent with the JPDF statistics in Fig. 12, showing large variations in reactivity of flat surfaces, since they are located differently (upstream and downstream) relative to the nearest leading edge. It is hypothesized that this behavior is caused by the historical effect of a passing leading edge and it reveals the critical role of flat surfaces in the global fuel consumption speed. Further exploration of this behavior requires future measurements of local thermal-chemical states conditioned on different flame typologies, which has recently become possible [5,17,30].

Another aspect highlighted by Fig. 12 is that increasing turbulence shifts ∇I_{OH} to higher magnitudes at moderate bulk velocities up to U_0 = 120 m/s, which then reduces towards the highest turbulence level at U_0 = 180 m/s. Since ∇I_{OH} is considered here as a qualitative marker for the local heat release rate, low-to-moderate turbulence enhances the local reaction speed, which is likely due to the combined effects of strain and curvature, as discussed previously ($S_b = S_L^0 - S_L^0 \kappa L_c - K_s L_s$). Further increased turbulence allows small eddies to penetrate and disturb the pre-heat zone, thus reducing the local ∇I_{OH}.

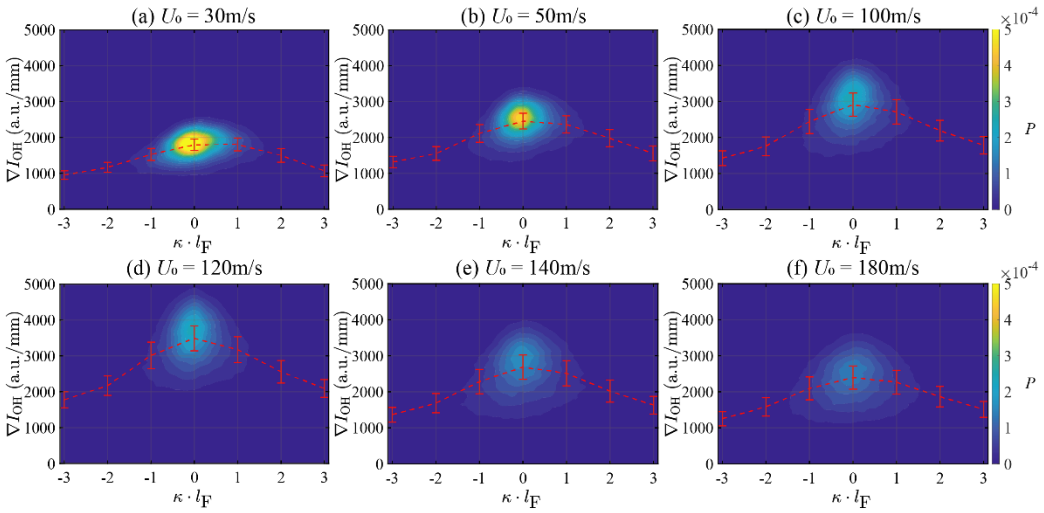

Fig. 12. Joint PDF of OH intensity gradient ∇I_{OH} and normalized flame surface curvature $\kappa \cdot l_F$ at *x*/D = 7 of purely premixed $NH_3/H_2/N_2$-air flames with increasing bulk velocity U_0. Red lines indicate mean values of ∇I_{OH}.

4.4 Main reaction thickness

To further explore the turbulence effect on the reaction zone, the characteristic length of the main reaction zone is evaluated based on the OH gradient, using the approach introduced in 1D strained flame simulations (Fig. 5). A threshold of 0.5 of the maximum ∇I_{OH} (FWHM) is applied along the flame normal direction to extract the OH layer thickness η_{OH}, as showcased in the previous examples in Fig. 11(d), where dashed lines indicate the FWHM thresholds. For statistical comparison, η_{OH} is conditioned on three different groups of absolute $\kappa \cdot l_F$ values, namely $|\kappa \cdot l_F| > 3$, $3 > |\kappa \cdot l_F| > 0.5$, and $|\kappa \cdot l_F| < 0.5$. They represent flame front topologies with strong, moderate, and low surface wrinkling.

Figure 13 illustrates the conditional mean η_{OH} with increasing bulk velocities from 10 to 180 m/s. The black dashed line represents η_{OH} from a 1D counterflow simulation with a low strain rate of 1,001/s. Although the flattened flame surfaces show a similar but slightly higher thickness than the low-strain simulation, a direct comparison to the simulation results is not intended. Overall, the experimental η_{OH} is larger than that from the counterflow flame due to several factors: 1) the curvature effect is still present, 2) the pilot flame has a preheating effect at low jet bulk velocities (resulting in longer residence times), and 3) the presence of OH radicals in the pilot flame increases the background intensity level. Therefore, the numerical η_{OH} should be considered a plausible reference rather than a basis for quantitative comparison.

Broader reaction zone layers are associated with higher curvature, increased by a factor of two for strongly curved surfaces at $|\kappa \cdot l_F| > 3$, although this difference rapidly decreases to about a factor of 0.5 as the strain rate increases. Still, this highlights the significant impact of curvature on thickening the reaction zone. Additionally, inspecting each $|\kappa \cdot l_F|$ group, η_{OH} shows consistently decreasing trends with increasing bulk velocity. This indicates how increasing strain associated with higher bulk velocities compresses the reaction zone into a narrow layer, which is in line with the simulation trend in Fig. 5(blue line). In contrast, turbulence has a minor influence on the OH layer thickness, clearly indicating that small eddies cannot penetrate and broaden the OH zone. This is because the HRR zone locates upstream of the OH zone, as observed in the 1D flame simulation in Fig. 4(b), and the turbulent kinetic energy is already strongly suppressed by the enhanced viscosity in front of the OH layer.

Figure 13(a-c) shows detailed OH gradient profiles along the flame normal direction $x \perp F$ for three selected bulk velocities of 10, 100, and 180m/s. The dashed lines indicate the ∇I_{OH} magnitude used to determine the OH layer FWHM thickness. These curvature-conditioned OH gradients suggest that highly curved flames have a broader OH layer with lower OH gradients, while less curved flames have a thinner layer with higher gradients. As the bulk velocity

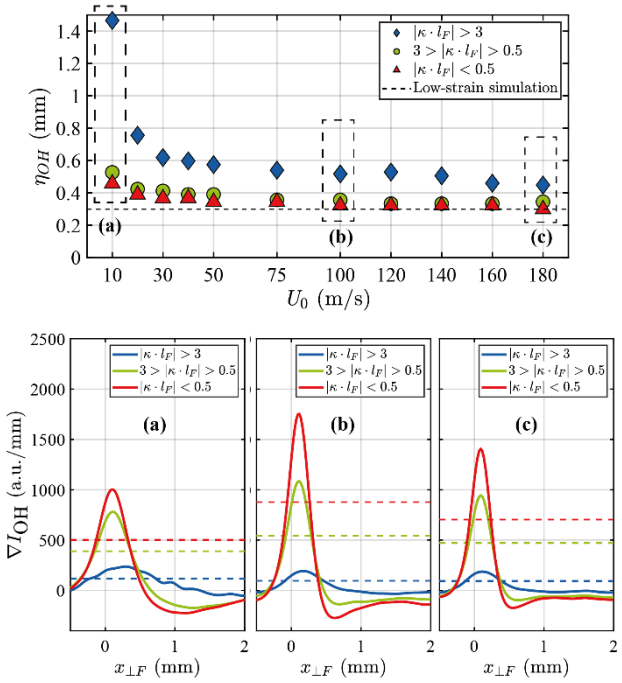

Fig. 13. The OH layer FWHM thickness η_{OH} of curved and flat flame region at x/D = 7 with increasing bulk velocity U_0. The value from 1D counter flow lame simulation at a low strain rate is plotted. Curvature-conditioned OH gradients ∇I_{OH} along the flame normal are shown for three different bulk velocities of 10, 100, and 180 m/s in (a-c), respectively.

increases from 10 to 180 m/s, the OH gradients exhibit an increase-then-decrease trend, consistent with the discussion in Fig. 12.

An in-depth characterization of local flame structures for lean turbulent $NH_3/H_2/N_2$-air flames is crucial for understanding global flame behavior such as flame extinction and turbulent flame speed S_T. For the latter, important flamelet parameters include flame surface area (σ), flame thickness, and stretch factor I_0 [38]. When *Le* is close to one, I_0 is close to unity, indicating an increased consumption rate due to enlarged reactive surface at low turbulent levels (Damköhler's first hypothesis), and flamelets propagate at the same speed as laminar flames. For a *Le* much smaller than one, I_0 can scale up to 2-6 for thermo-diffusively unstable flames [37]. The large stretch factor is attributed to the local fuel focusing effect, burning rate enhancement near leading edges, and the enlarged effective surface of a thermo-diffusively unstable reaction front. Quantitative experiments are still lacking to clearly reveal the complex interaction mechanism between global turbulent burning speed and local thermo-chemical states (temperature vs. fuel mole fraction). Moreover, it is challenging for simulations to account for different types of flamelets, especially those driven by differential diffusion, to predict the correct global burning rate.

Concerning the current flame set, it is demonstrated that flames with low curvatures ($|\kappa \cdot l_F| < 0.5$) exhibit a similar thickness compared to corresponding laminar flames, thus are not significantly broadened by turbulence. Note that the OH gradient is used to describe the thickness of the main reaction zone, while the pre-heat zone could still be thickened with the penetration of turbulent eddies. This observation is also supported by a recent study [16], showing significantly different responses of scalars such as NH_3, NH, and OH to turbulence disturbance, as they peak at different locations within the pre-heat and main reaction zone. Additionally, low flame curvature dominates the flame topology characteristics of the current lean premixed flames even at extreme turbulence. Since flat flame structures are associated with high reaction rates marked by ∇I_{OH}, we hypothesize that these structures may dominate the global burning behavior, instead of leading edges, which appear at lower probability and reduced reactivity. Strongly curved flame surfaces ($|\kappa \cdot l_F| > 3$) are substantially thicker, as they exist at the limit to local extinction.

5. Conclusions

In the present work a set of lean premixed turbulent $NH_3/H_2/N_2$-air jet flames was studied with increasing jet bulk velocities ranging from 30 to 180 m/s at a constant equivalence ratio ϕ_{global} = 0.57. These flames are classified within the transition from thin reaction zones to the distributed burning regime, covering a wide range of Ka from approximately 75 to 2,140, based on turbulent velocities and integral length scales derived from PIV measurements. 1D simulations of strained counterflow flames reveal that OH radical gradients are spatially correlated but located downstream of the HRR zone. 1D strained flame simulations suggest an increasing burning speed and decreasing OH layer thickness with rising strain rates. Building upon the understanding from these simulations, turbulent flow and flame characteristics are characterized with simultaneous single-shot PIV and OH-LIF measurements. Several key observations and conclusions are summarized as follows.

(1) The flame surface marked by OH is increasingly disturbed by turbulence as turbulent eddies with higher kinetic energy gradually penetrate the reaction zone, smearing the OH-LIF intensities and gradients. Turbulence primarily shapes the flame surface density (FSD) and κ (curvature) probability distribution, while differential diffusion has a marginal role at high turbulence levels.

(2) The OH intensity gradient ∇I_{OH} serves as a marker for local reactivity and thermo-diffusive instabilities. Positively curved surfaces consistently show higher ∇I_{OH} than negatively curved counterparts due to the differential diffusion effect of H_2. This discrepancy is reduced at higher *Ka* numbers, where turbulent transport dominates the mixing process.

(3) Flat flame surfaces are always the majority among all different surface topologies; however, this topology is associated with significant discrepancies in local flame reactivity marked by ∇I_{OH}. It is because flattened surfaces frequently exist before and after leading edges, playing an essential role in the local fuel consumption rate.

(4) The mean reaction zone thickness η_{OH} significantly enlarges at strongly curved flame zones. While strain compresses the reaction zone into a narrow layer, turbulence has a minor influence on the OH layer thickness, indicating that small eddies cannot penetrate and broaden the OH layer, as it exists downstream of the HRR zone.

Acknowledgments

We are grateful for financial support by the DFG, project number 503997890. T. Li acknowledges the financial support by the Fritz und Margot Faudi-Stiftung. A. Dreizler was financially supported by the Gottfried Wilhelm Leibniz-Preis (DFG). B. Zhou acknowledges support by the NSFC Grant (No. 52206150).

Conflicts of Interest

The authors declare no conflict of interest.

References

[1] Davis J.S., et al. Net-zero emissions energy systems, Science (New York, N.Y.) 360 (2018), https://doi.org/10.1126/science.aas9793
[2] Valera-Medina A., Xiao H., Owen-Jones M., David W., Bowen P.J. Ammonia for power, Prog Energy Combust Sci 2018, 69: 63–102. https://doi.org/10.1016/j.pecs.2018.07.001
[3] Kobayashi H., Hayakawa A, Somarathne K.K.A., Okafor E.C. Science and technology of ammonia combustion, Proc Combust Inst 2019, 37: 109–133. https://doi:10.1016/j.proci.2018.09.029
[4] Ju Y., Sun W. Plasma assisted combustion: Dynamics and chemistry, Prog Energy Combust Sci 2015, 48: 21–83. https://doi:10.1016/j.pecs.2014.12.002
[5] Schultheis R., Li T., Shi S., Barlow R.S., Zhou B., Geyer D., Dreizler A. Quantitative measurements of thermo-chemical states in turbulent lean and rich premixed NH3/H2/N2-air jet flames, Proc Comb Inst 2024, 40: 105571, https://doi:10.1016/j.proci.2024.105571
[6] Li T., Doğrudil M., Dreizler A. Macroscopic flame and flow structures in hydrogen and methane multi-regime combustion, Proc Combust Inst 2024, 40:105759, https://doi:10.1016/j.proci.2024.105759
[7] Tang H., Yang C., Wang G., Krishna Y., Guiberti T.F., Roberts W.L., Magnotti G. Scalar structure in turbulent non-premixed NH3/H2/N2 jet flames at elevated pressure using Raman spectroscopy, Combust Flame 2022, 244: 112292, https://doi:10.1016/j.combustflame.2022.112292
[8] Cai X., Fan Q., Bai X.-S., Wang J., Zhang M., Huang Z., Alden M., Li Z. Turbulent burning velocity and its related statistics of ammonia - hydrogen - air jet flames at high Karlovitz number: Effect of differential diffusion, Proc Combust Inst 2023, 39: 4215–4226, https://doi:10.1016/j.proci.2022.07.016
[9] Wiseman S., Rieth M., Gruber A., Dawson J.R., Chen J.H. A comparison of the blow-out behavior of turbulent premixed ammonia/hydrogen/nitrogen-air and methane–air flames, Proc Combust Inst 2021, 38: 2869–2876, https://doi:10.1016/j.proci.2020.07.011
[10] Wei X., Zhang M., Wang J., Huang Z. Investigation on lean blow-off characteristics and stabilization mechanism of premixed hydrogen enhanced ammonia/air swirl flames in a gas turbine combustor, Combust. Flame 2023, 249: 112600, https://doi:10.1016/j.combustflame.2022.112600
[11] Alfazazi A., Elbaz A.M., Li J., Abdelwahid S., Im H.G., Dally B. Characteristics of ammonia-hydrogen nonpremixed bluff-body-stabilized flames, Combust Flame 2023, 258: 113066, https://doi:10.1016/j.combustflame.2023.113066.
[12] Peters N. Turbulent Combustion, Meas Sci Technol 2022, 12. https://doi:10.1088/0957-0233/12/11/708
[13] Fan Q., Liu X., Xu L., Subash A.A., Brackmann C., Aldén M., Bai X.-S., Li Z. Flame structure and burning velocity of ammonia/air turbulent premixed flames at high Karlovitz number conditions, Combust Flame 2022, 238: 111943, https://doi:10.1016/j.combustflame.2021.111943
[14] Ichikawa A., Hayakawa A., Kitagawa Y., Somarathne K.D.D.A., Kudo T., Kobayashi H. Laminar burning velocity and Markstein length of ammonia/hydrogen/air premixed flames at elevated pressures, Int J Hydro Energy 2015, 40: 9570–9578, https://doi:10.1016/j.ijhydene.2015.04.024
[15] Li X., Wang Z., Li T., Dreizler A., Lipatnikov A.N., Liu X., Gan X., Zhou B. Investigation of burning velocity of lean and rich premixed NH3/H2 turbulent flames using multi-scalar imaging, Proc Combust Inst 2024, 40: 105541, https://doi:10.1016/j.proci.2024.105541
[16] Wang Z., Li X., Li T., Dreizler A., Lipatnikov A.N., Liu X., Gan X., Zhou B. Experimental investigation of internal structures of NH3/H2/O2/N2 premixed jet flames using multi-scalar imaging, Proc Combust Inst 2024, 40: 105436, https://doi:10.1016/j.proci.2024.105436
[17] Shi S., Schultheis R., Barlow R.S., Geyer D., Dreizler A., Li T. Internal flame structures of thermo-diffusive lean premixed H2/air flames with increasing turbulence, Proc Combust Inst 2024, 40: 105225, https://doi:10.1016/j.proci.2024.105225
[18] Zhou B., Brackmann C., Li Q., Wang Z., Petersson P., Li Z. Aldén M., Bai X.-S. Distributed reactions in highly turbulent premixed methane/air flames, Combust Flame 2015, 162: 2937–2953, https://doi:10.1016/j.combustflame.2014.12.021
[19] Han X., Wang Z., He Y., Zhu Y., Cen K. Experimental and kinetic modeling study of laminar burning velocities of NH3/syngas/air premixed flames, Combust Flame 2020, 213: 1–13, https://doi:10.1016/j.combustflame.2019.11.032
[20] Poinsot T. Theoretical and numerical combustion, 2nd ed., Edwards, Philadelphie, 2005.
[21] Bouvet N., Halter F., Chauveau C., Yoon Y. On the effective Lewis number formulations for lean hydrogen/hydrocarbon/air mixtures, Int J Hydro Energy 2013, 38: 5949–5960, https://doi:10.1016/j.ijhydene.2013.02.098
[22] Addabbo R., Bechthold J.K., Matalon M. Wrinkling of spherically expanding flames, Proc Combust Inst 2002, 29: 1527–1535, https://doi:10.1016/s1540-7489(02)80187-0
[23] Bechthold J.K., Malaton M. The dependence of the Markstein length on stoichiometry, Combust

Flame 2001, 127: 1906–1913, https://doi:10.1016/s0010-2180(01)00297-8
[24] Alnasif A. et al. Evolution of ammonia reaction mechanisms and modeling parameters: A review, Appl Energy Combust Sci 2023, 15: 100175, https://doi:10.1016/j.jaecs.2023.100175
[25] Girhe S., Snackers A., Lehmann T., Langer R., Loffredo F., Glaznev R., Beeckmann J., Pitsch H. Ammonia and ammonia/hydrogen combustion: Comprehensive quantitative assessment of kinetic models and examination of critical parameters, Combust Flame 2024, 267: 113560, https://doi:10.1016/j.combustflame.2024.113560
[26] Chaib O., Hochgreb S., Boxx I. An experimental marker of thermo-diffusive instability in hydrogen-enriched flames, Proc Combust Inst 2024, 40: 105763, https://doi.org/10.1016/j.proci.2024.105763
[27] Chaib O., Zheng Y., Hochgreb S., Boxx I. Hybrid algorithm for the detection of turbulent flame fronts, Exp Fluids 2023, 64: 104, https://doi:10.1007/s00348-023-03651-6
[28] Li T., Zhou B., Frank J.H., Dreizler A., Böhm B. High-speed volumetric imaging of formaldehyde in a lifted turbulent jet flame using an acousto-optic deflector, Exp Fluids 2020, 61. https://doi:10.1007/s00348-020-2915-y
[29] Law C., Sung C. Structure, aerodynamics, and geometry of premixed flamelets, Prog Energy Combust Sci 2000, 26: 459–505, https://doi:10.1016/S0360-1285(00)00018-6
[30] Shi S., Schultheis R., Barlow R.S., Geyer D., Dreizler A., Li T., Schultheis R. Assessing turbulence-flame interaction of thermo-diffusive lean premixed H2/air flames towards distributed burning regime, Combust Flame 2024, 269: 113699, https://doi:10.1016/j.combustflame.2024.113699
[31] Aspden A.J., Day M.S., Bell J.B. Lewis number effects in distributed flames, Proc Combust Inst 2011, 33: 1473–1480, https://doi:10.1016/j.proci.2010.05.095
[32] Bray K.N.C., Cant R.S. Some applications of Kolmogorov's turbulence research in the field of combustion, Proc R Soc Lond A 1991, 434: 217–240, https://doi:10.1098/rspa.1991.0090
[33] Savitzky A., Golay M.J.E. Smoothing and Differentiation of Data by Simplified Least Squares Procedures, Anal Chem 1964, 36: 1627–1639, https://doi:10.1021/ac60214a047
[34] Howarth T.L., Hunt E.F., Aspden A.J. Thermodiffusively-unstable lean premixed hydrogen flames: Phenomenology, empirical modelling, and thermal leading points, Combust Flame 2023, 253: 112811, https://doi:10.1016/j.combustflame.2023.112811
[35] Aspden A.J., Day M.S., Bell J.B. Turbulence–flame interactions in lean premixed hydrogen: transition to the distributed burning regime, J Fluid Mech 2011, 680: 287–320, https://doi:10.1017/jfm.2011.164
[36] Lipatnikov A.N., Chomiak J. Molecular transport effects on turbulent flame propagation and structure, Prog Energy Combust Sci 2005, 31: 1–73, https://doi:10.1016/j.pecs.2004.07.001
[37] Ahmed P., Thorne B., Lawes M., Hochgreb S., Nivarti G.V., Cant R.S. Three dimensional measurements of surface areas and burning velocities of turbulent spherical flames, Combust Flame 2021, 233: 111586, https://doi:10.1016/j.combustflame.2021.111586